JOURNAL OF GEOPHYSICAL RESEARCH, VOL. 113, B10308, doi:10.1029/2007JB005306, 2008

Nature of the crust beneath northwest Basin and Range province from teleseismic receiver function data

Ewenet M. Gashawbeza,[1] Simon L. Klemperer,[1] Charles K. Wilson,[1,2] and Elizabeth L. Miller[3]

Received 30 July 2007; revised 12 April 2008; accepted 2 July 2008; published 14 October 2008.

[1] We utilized teleseismic receiver function techniques complemented by active source refraction seismology to study the crustal structure and continental rift processes responsible for the development of the northwest corner of the Basin and Range province in northwest Nevada. Our passive seismic array of 28 short-period stations, spanning 70 km west to east, and 5 broadband USArray transportable array stations that extended our aperture to 230 km provided data on crustal properties independent of the results of our active source refraction experiment. Combining data from the two experiments provides better constraints on Moho depth, V_p/V_s ratio, and the structure and composition of the crust beneath the northwestern Basin and Range province than possible from either experiment alone. Our new data indicate Moho depths that vary from 29.5 on the east to 36.5 km in the west along the passive source array and V_p/V_s ratios that systematically span a wide range from 1.68 to 1.83. Velocity modeling of data collected from the 300 km, wide-angle refraction/reflection survey provides comparable Moho depths of 32–37 km under the same region. Decreasing V_p/V_s is correlated with decreasing crustal thickness, with V_p/V_s ratio > 1.80 in northeast California and $V_p/V_s < 1.74$ in the thinner crust of the Basin and Range province. We associate the high V_p/V_s of northeast California with mafic additions to the crust during formation of the Modoc Plateau in a region of accreted Paleozoic island arc terrans similar to those exposed in the eastern Klamaths and northwestern Sierra Nevada. Unusually low V_p/V_s in conjunction with low absolute V_p and V_s is observed beneath the central part of our array and may be due to the roots of the Sierra Nevada batholith, now dismembered by Basin and Range faults. Back azimuthal stacking of our receiver function data suggests a northwest oriented crustal anisotropy fast direction beneath this region, parallel to the northwest to southeast oriented Cenozoic extension experienced by the Basin and Range province and suggestive of a similar flow direction in the middle to lower crust.

Citation: Gashawbeza, E. M., S. L. Klemperer, C. K. Wilson, and E. L. Miller (2008), Nature of the crust beneath northwest Basin and Range province from teleseismic receiver function data, *J. Geophys. Res.*, *113*, B10308, doi:10.1029/2007JB005306.

1. Introduction

1.1. Regional Tectonic History

[2] The Basin and Range province of western North America is one of the best regions in the world for the study of processes related to continental rifting. It is a broad and elevated region of intracontinental stretching with high heat flow [*Blackwell et al.*, 1991] extending in a "wide rift" mode [e.g., *Buck*, 1991; *Thatcher et al.*, 1999] between the stable blocks of the Sierra Nevada to the west and the Colorado Plateau to the east. It is also a region underlain by relatively thin crust despite seismic and petrologic evidence for mafic underplating during rift-related magmatism [e.g., *Klemperer et al.*, 1986; *Christiansen and Yeats*, 1992].

[3] As part of the tectonic evolution of the North American Cordilleran, northwest Nevada has had a complex tectonic history. In Late Proterozoic or earliest Paleozoic time, breakup of the supercontinent Rodinia [e.g., *Dalziel*, 1997] led to the development of a west facing passive margin at the rifted edge of Precambrian continental crust. This rifted edge has commonly been located through north central Nevada using the 0.706 isopleth of initial $^{87}Sr/^{86}Sr$ ratios [*Kistler and Peterman*, 1978; *Kistler*, 1990] (Figure 1).

[4] During the Late Devonian to Early Mississippian Antler orogeny, coeval eugeoclinal siliciclastic rocks were thrust eastward over rocks of the continental shelf. Accretion of oceanic terranes continued during the late Permian to Early Triassic time during the Sonoma orogeny [*Miller et al.*, 1992]. The Sonoma orogeny culminated in the accretion

[1]Department of Geophysics, Stanford University, Stanford, California, USA.
[2]Now at Marsico Capital Management, Denver, Colorado, USA.
[3]Department of Geological and Environmental Sciences, Stanford University, Stanford, California, USA.

0148-0227/08/2007JB005306$09.00

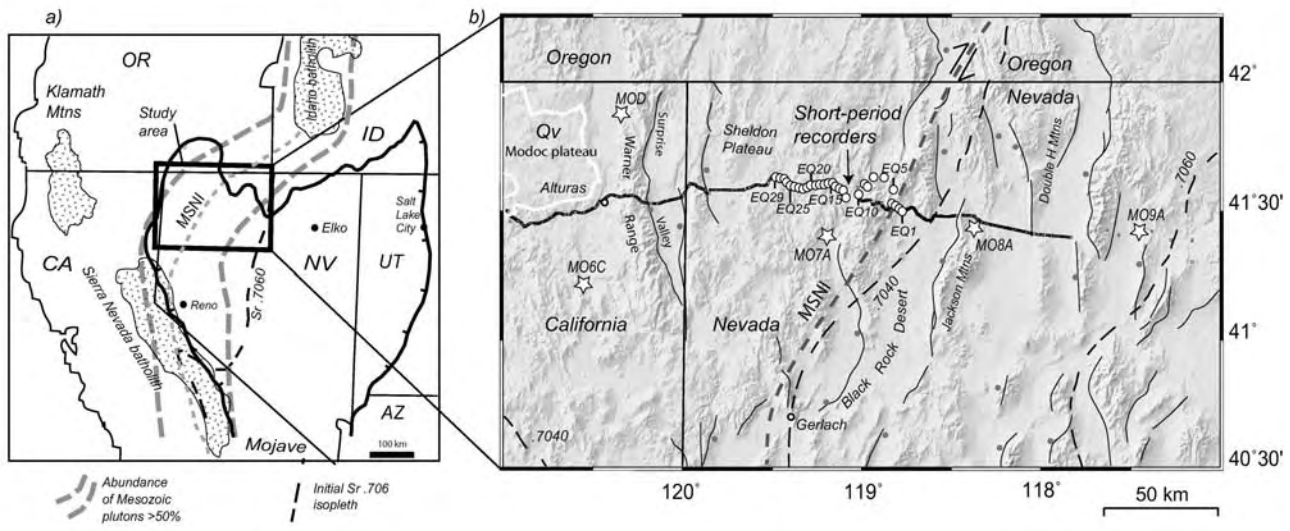

Figure 1. (a) Map of western United States, showing location of study area (black square) in Basin and Range province (heavy black outline with barbs) and approximate extent of Cretaceous batholith (zone of >50% Mesozoic plutons from *Barton and Hanson* [1989]). (b) Detailed map of experiment layout superimposed on shaded relief topography. Stars are USArray transportable array broadband stations. Large white circles are short-period recorders numbered EQ1 to EQ29. Small white squares are seismographs for the refraction line (typically spaced at ~300 m, so white squares form a continuous line). Gray dashed line is the Mojave-Snow-Nevada-Idaho Shear Zone (MSNI) [*Wyld and Wright*, 2001]. Black dashed line is Sr^{87}/Sr^{86} 0.7040 and 0.7060 isopleths [*Pierce et al.*, 2002]. Qv and white line are Quaternary volcanics of the Modoc Plateau. Thin black lines are normal faults with balls on the downthrown side. The inset map locates the project area with respect to the California/Nevada/Oregon state map, the Sierra Nevada and Idaho batholith and the Klamath mountains (crosshatched).

of oceanic terranes and the establishment of an active continental margin west of Nevada [*Burchfiel et al.*, 1992]. Deformation, crustal thickening, and magmatism related to the active continental margin to the west continued during Mesozoic time [*Burchfiel et al.*, 1992].

[5] Predominantly Cretaceous granitic plutons similar to the presently exposed Sierra Nevada batholith intruded the Paleozoic and early Mesozoic rocks of northwestern Nevada. These plutons are believed to be contiguous with the main Sierra Nevada batholith [*Burchfiel and Davis*, 1975; *Wyld and Wright*, 2001]. The Cretaceous Sierra Nevada batholith is a magmatic arc emplaced into an older metamorphic framework, broadly along the line separating Paleozoic and Mesozoic oceanic terranes to the west from North American Proterozoic lithosphere to the east [*Burchfiel and Davis*, 1975].

[6] The beginning of Tertiary time marked a transition to extensional tectonics, characterized primarily by magmatism, regional uplift, the formation of the northern Nevada rift, and widespread development of tilted fault blocks and intervening valleys (Basin and Range features) in the late Tertiary [*Christiansen and Yeats*, 1992].

[7] Basin and Range extension in northwestern Nevada is relatively younger (<12 Ma), and smaller in magnitude (<20%) [e.g., *Colgan et al.*, 2006] compared to the central portion of Nevada (<30 Ma) which extended (50–100%). Basaltic volcanism began to dominate this region about 16–17 Ma [*Pierce et al.*, 2002]. Beginning ~8 Ma and continuing to the present, magmatism has migrated to the margins of the Basin and Range province [*Parsons*, 1995] while NW-SE extension, characterized by high-angle block faulting, dominates in the northwestern and central Basin and Range [e.g., *Parsons*, 1995].

1.2. Previous Shear Wave Speed Measurements

[8] Only the gross shear wave structure of the crust and upper mantle of the northern Basin and Range province has been determined on the basis of regional surface wave phase velocity data inversions [e.g., *Priestley and Brune*, 1978, 1982; *Priestley et al.*, 1980; *Taylor and Patton*, 1986]. In contrast, modern reflection and refraction profiles have revealed more details of compressional wave crustal structure [e.g., *Klemperer et al.*, 1986; *Allmendinger et al.*, 1987; *Potter et al.*, 1987; *Holbrook*, 1990; *Catchings and Mooney*, 1991; *Lerch et al.*, 2007]. One-dimensional shear wave structures obtained from the inversion of receiver functions have the potential to offer vertical and horizontal resolution comparable to the compressional wave structures obtained from refraction studies [*Zandt and Owens*, 1986]. At a given frequency, shear waves have shorter wavelengths than compressional waves and thus maintain higher resolution; a crustal shear wave with a dominant frequency of 1 Hz is influenced by layers as thin as 1 km [*Owens*, 1987]. Shear waveforms also display stronger anomalies than compressional waveforms because of seismic anisotropy, fluids and fractures in crustal rocks, and partial melt in the upper mantle. With high-quality receiver functions, these aspects

of the crust can be studied in more detail than the P wave data alone.

[9] Better crustal composition inferences can be made from the V_p/V_s ratio and its derived elastic parameter σ (Poisson's ratio) than by utilizing compressional or shear velocities separately. This has been effectively demonstrated by laboratory experiments [e.g., *Kern*, 1982; *Christensen*, 1996]. *Christensen* [1996] recognized the difficulty of obtaining good resolution of σ based on V_p and V_s derived from refraction experiments, despite some studies that have shown good agreement of laboratory and refraction velocity data [e.g., *Salisbury and Fountain*, 1993]. Experimental data [*Kern*, 1982; *Christensen*, 1996] show σ mainly depends on rock composition rather than on P-T conditions [*Tarkov and Vavakin*, 1982], although some studies [e.g., *Christensen*, 1996] have shown that increasing metamorphic grade has a significant effect and increases V_p/V_s. Fluid phases and partial melts also have a significant influence in reducing seismic velocities, as shown by *Watanabe* [1993] for ultramafic rocks.

[10] Values of V_p/V_s for common crustal and mantle rocks lie between 1.73 and 1.87 (σ between 0.25 and 0.30), except for four lithologies: serpentinite (2.08), anorthosite (1.9), granite-granodiorite (1.66), and quartzite (1.5) [*Christensen*, 1996]. Experimental data [*Kern*, 1982; *Christensen*, 1996] show V_p/V_s increases as quartz content decreases from granite to gabbro. V_p/V_s decreases as rocks become ultramafic in composition as plagioclase content decreases. Both V_p and V_s increase with increasing proportion of mafic minerals such as amphibole, pyroxene and olivine.

[11] An early global compilation of average values of crustal V_p/V_s ratio from receiver function analysis of teleseismic data [*Zandt and Ammon*, 1995] found $V_p/V_s = 1.78$ and 1.83 (σ = 0.27 and 0.29) for platforms and shields, respectively. V_p/V_s for Mesozoic-Cenozoic orogenic belts is lower, ~1.73 and the highest values, ~1.91, were found for island arcs [*Zandt and Ammon*, 1995]. *Ramesh et al.* [2002] obtained average V_p/V_s values of 1.76 (σ = 0.26) for both the North American Cordillera and for Archean domains of Canada and concluded that σ may be less dependent on crustal age than on the composition and processes involved in the crust formation.

1.3. Receiver Function Methodology

[12] With the receiver function technique, teleseismic body waves are used to image crustal structure beneath individual seismic stations. These waveforms contain information related to the earthquake source time function, its propagation through the mantle, and local structures beneath the recording site. The resulting receiver function is obtained by removing the effects of source function and its path through the mantle.

[13] The basis of this method is that part of the P wave signal from distant events that is incident on a discontinuity in the crust or upper mantle will be converted to S waves (Ps) that arrive at the station shortly after the direct P wave. Because the S waves travel more slowly than the P waves, the depth of the discontinuity can be calculated from the time difference in the arrival of the direct P wave and the converted phase (Ps), provided that the velocity structure is known. Extracting these converted phases from the P wave coda requires several processing steps, including rotation into the ray coordinate system, deconvolution [*Phinney*, 1964; *Vinnik*, 1977] and stacking of the receiver functions [*Zhu and Kanamori*, 2000]. Variability in Ps delay time and amplitude among stations carries useful information about the lateral variation of crustal properties or anisotropy.

2. New Seismic Data

[14] In this study we used 8 months of teleseismic data recorded on 29 PASSCAL seismographs equipped with L22 (2 Hz) sensors spaced at ~2.5 km spanning a total distance of ~70 km, supplemented by data from the 4 closest USArray transportable broadband stations and one Berkeley digital station (Figure 1 and Table 1). The PASSCAL recorders were embedded within a 300 km controlled source refraction profile described by *Lerch et al.* [2007]. 480 teleseismic events were recorded, of which we utilized those 290 events with an epicentral distance from 30° to 110° and magnitudes >5.5 (Figure 2). We computed receiver functions using a time domain iterative deconvolution algorithm [*Ligorria and Ammon*, 1999]. The typical frequency range recorded by our short-period instruments was 0.5–10 Hz and the dominant frequency is 2 Hz. We applied band-pass filtering from 0.2 to 2 Hz to the short–period waveforms and from 0.1 to 2 Hz for the broadband USArray data. Following testing of Gaussian filter values from 2 to 10 [*Langston*, 1979] we computed about 4000 receiver functions using Gaussian values of 2.5 for the broadband data and Gaussian values of 5 for short-period data. We visually inspected each receiver function, sorting them by back azimuth (Figure 3b) and incident angle (Figure 3c) and comparing them with neighboring stations. Receiver functions with weird shapes and amplitudes on either radial or tangential components were discarded. We finally utilized a total of 1042 receiver functions for the 28 short-period stations and 309 receiver functions for the 5 broadband stations, and for each receiver made stacked sections for all events as a function of both back azimuth and slowness (e.g., Figure 3).

[15] The Ps Moho phase is clearly visible on all radial receiver functions at all back azimuths. For example in station M07A (Figure 3b) it occurs at a delay time of ~4.1 s at most azimuths and becomes a doublet for receiver functions from events from southeasterly back azimuths. Meaningful back azimuthal variation can only be assessed for the USArray stations that have the largest number of earthquakes. A similar variation with a doublet Moho for arrivals from the southeast is seen for stations M06C and M08A, but is not present on MOD. Its existence cannot be assessed for our other stations. Variability in Ps delay time and amplitude among stations carries useful information about the lateral variation of crustal properties or anisotropy. For example, simple station stacks across the short-period recorders show larger delay times for the western stations (Figure 4). There is also noticeable amplitude and frequency change, both for direct P, and for the Moho conversion, between stations EQ12 and EQ10 presumably due to laterally varying geology (EQ11 recorded no useful data). The difference in sharpness of the Moho conversion could be due to changes in the gradient of velocity change with

Table 1. Station Names, Locations, Elevation, Crustal Thickness and V_p/V_s Ratio From H-k Stacks, Number of Receiver Functions Calculated and Data Quality for All Stations Arranged West to East[a]

Station	Latitude (deg)	Longitude (deg)	Elevation(m)	H (km)	V_p/V_s	Receiver Functions	Rank[b]
TA/M06C	41.2050	−120.4770	1434	34.50 ± 0.5	1.83 ± 0.03	85	A
BK/MOD	41.9024	−120.3029	1554	36.50 ± 0.2	1.82 ± 0.01	150	A
EQ29	41.6336	−119.4792	1801	34.52 ± 1.3	1.77 ± 0.03	40	A
EQ28	41.6286	−119.4560	1790	33.62 ± 1.3	1.75 ± 0.04	35	B
EQ27	41.6265	−119.4321	1801	34.36 ± 2.3	1.69 ± 0.04	15	B
EQ26	41.6134	−119.4184	1752	32.86 ± 1.3	1.79 ± 0.03	33	B
EQ25	41.6007	−119.3983	1659	33.50 ± 0.4	1.76 ± 0.02	33	A
EQ24	41.5954	−119.3751	1761	33.26 ± 1.5	1.79 ± 0.03	38	B
EQ23	41.5917	−119.3512	1812	33.59 ± 1.2	1.79 ± 0.03	13	A
EQ22	41.5873	−119.3273	1868	33.35 ± 0.3	1.76 ± 0.03	55	B
EQ21	41.5925	−119.3045	1374	33.48 ± 0.2	1.72 ± 0.03	21	B
EQ20	41.6019	−119.2848	1877	31.94 ± 0.2	1.72 ± 0.01	40	B
EQ19	41.6016	−119.2576	1822	32.56 ± 1.0	1.72 ± 0.02	41	A
EQ18	41.6051	−119.2338	1877	33.42 ± 1.2	1.75 ± 0.01	27	B
EQ17	41.6045	−119.2095	1877	-	-	21	C
EQ16	41.6090	−119.1860	1777	-	-	42	C
TA/M07A	41.3884	−119.1711	1400	32.50 ± 0.5	1.74 ± 0.01	60	A
EQ15	41.6106	−119.1614	1729	-	-	-	C
EQ14	41.5968	−119.1460	1733	33.05 ± 1.04	1.75 ± 0.02	46	B
EQ13	41.5890	−119.1245	1796	-	-	46	C
EQ12	41.5817	−119.1024	1759	-	-	45	C
EQ11	41.5534	−119.0879	1763	did not record	useful data	-	C
EQ10	41.5654	−119.0180	1821	-	-	40	C
EQ9	41.6059	−118.9852	1800	-	-	29	C
EQ8	41.5955	−118.9673	1843	33.50 ± 1.0	1.75 ± 0.04	62	B
EQ7	41.6324	−118.9334	1643	32.49 ± 0.3	1.72 ± 0.05	27	A
EQ6	41.6320	−118.8738	1405	-	-	60	C
EQ5	41.5845	−118.8226	1500	-	-	51	C
EQ4	41.5304	−118.8320	1525	-	-	36	C
EQ3	41.5208	−118.8109	1418	30.50 ± 1.6	1.68 ± 0.04	17	A
EQ2	41.5095	−118.7911	1299	31.04 ± 2.3	1.78 ± 0.04	22	B
EQ1	41.4996	−118.7737	1240	-	-	70	C
TA/M08A	41.4483	−118.3792	1288	29.50 ± 0.5	1.75 ± 0.01	65	A
TA/M09A	41.4230	−117.4497	1356	30.20 ± 0.8	1.77 ± 0.01	21	A

[a]Stations prefixed M0 are USArray broadband stations; station MOD is from the Berkeley digital seismograph network; stations named EQ are short-period PASSCAL instruments.
[b]A is best, C is worst.

depth or could possibly be due to interference of other arrivals with the Moho arrival making it look broader on some of the eastern stations (Figure 4).

3. Receiver Function Inversion

[16] Receiver functions can be inverted for shear velocity structure under a given seismic station [*Ligorria and Ammon*, 1999] by minimizing the difference between observed and synthetic receiver functions [*Ozalaybey et al.*, 1997]. Because there is no guarantee that a unique inversion result will be obtained, using available a priori information is helpful in constraining the solutions. We utilized two inversion techniques, the *Zhu and Kanamori* [2000] "H-k" stacking algorithm and the neighborhood algorithm technique of *Sambridge* [1999], to derive constraints on crustal velocities for our study area. In both techniques we have implicitly assumed an isotropic seismic structure of the crust and upper mantle composed of flat-lying planar interfaces.

3.1. H-k Stacking

[17] We employed the H-k stacking algorithm of *Zhu and Kanamori* [2000] for simultaneous determination of crustal thickness (H), and V_p/V_s ratio (k). This algorithm stacks the

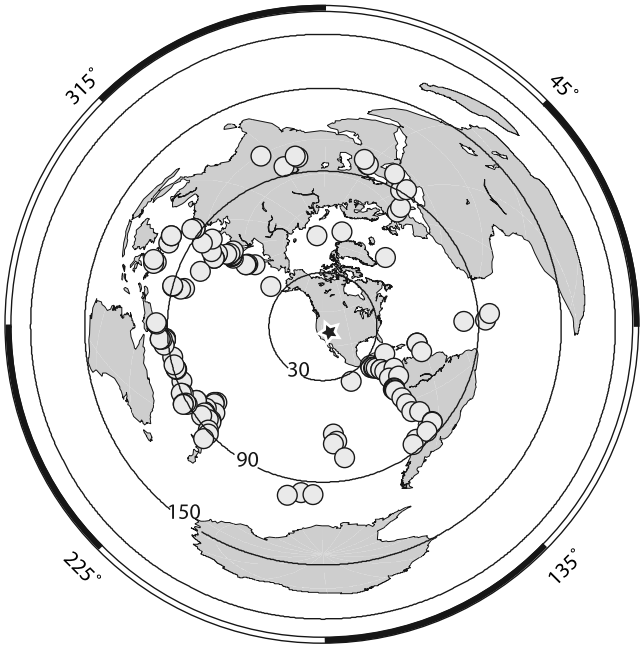

Figure 2. Location of 290 teleseismic events used in this study (m_b > 5.5 and epicentral distance between 30° and 110°).

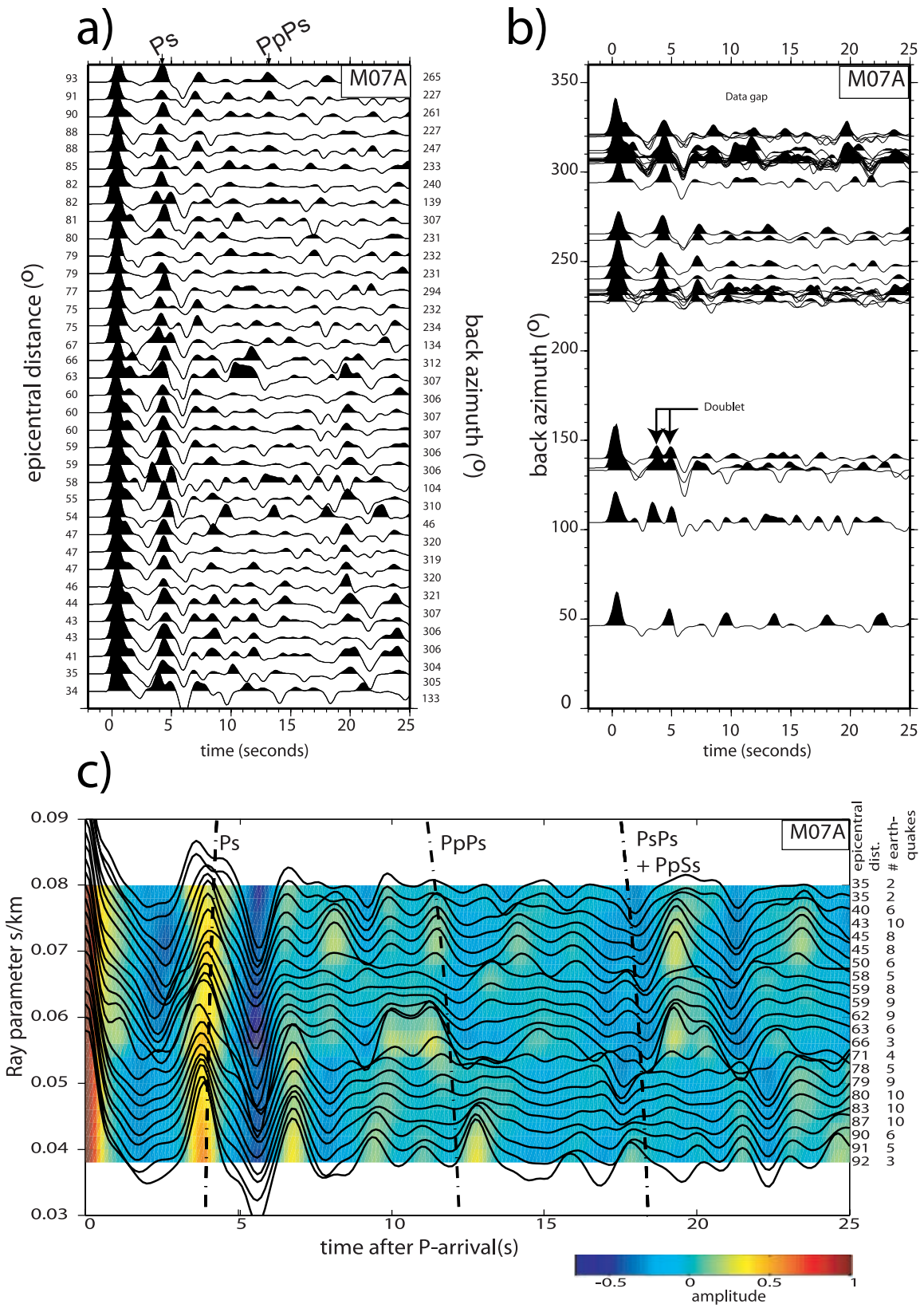

Figure 3. Receiver functions at station M07A (a) sorted by epicentral distance, (b) plotted as a function of back azimuth and (c) plotted as a function of ray parameter. Dashed lines in Figure 3c represent arrival times of the Moho Ps and its multiples PpPs and PsPs + PpSs calculated for a 32.5 km thick crust and P wave velocities from wide-angle refraction data [*Lerch et al.*, 2007]. Data in Figure 3c are binned and stacked within ray parameter increments of 0.002. The right vertical axis shows the average delta in each bin and number of receiver functions used in each ray parameter bin.

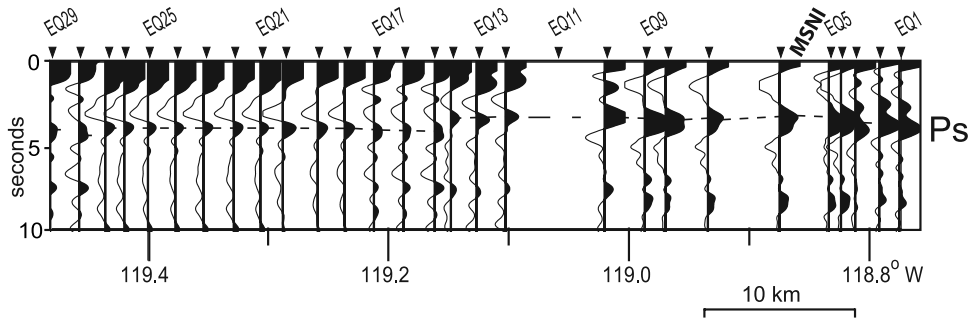

Figure 4. Stacked receiver functions for each short-period station to show Ps delay time variation across the short-period stations. We used the one-dimensional IASP91 velocity model to calculate moveout corrections before creating these simple station stacks. Dashed line is Moho delay time pick. Note that even within the short-period array, spanning just ~70 km west to east, we observed variation in Moho delay times. MSNI; Mojave-Snow-Nevada-Idaho shear zone.

amplitudes of receiver functions at the predicted arrival time for the Moho conversion (Ps) and its multiples (PpPs and PpSs + PsPs, see Figure 3c) for different crustal thicknesses and V_p/V_s ratios (Figure 5). The advantage of this method is that there is no need to subjectively pick the arrival times of the direct conversion from the Moho and its multiples.

[18] At all five broadband stations, the Moho P-to-S converted phase Ps and its multiples PpPs and PpSs + PsPs can be clearly identified. For many of the short-period data, it is difficult to see the multiple phases clearly, presumably because of the reverberations in the sedimentary section and other high-frequency noise. At some of the stations, these basin reverberations obscure the Moho converted phases and prevent accurate determination of crustal thickness beneath these stations. We classified stations on the basis of the quality of the original receiver functions (Table 1). Those in category A (four USArray stations, one permanent Berkeley station and six short-period stations) display a clear Moho Ps conversion in the time window of 3.5–5 s, and also show the two multiples PpPs and PpSs + PsPs near the predicted arrival times (calculated using $V_p/V_s = 1.73$; see Figure 3c for example). For most of the category A stations, a well-defined peak on the H-k plot is consistently observed, and therefore both H and V_p/V_s can be determined with high confidence. The 11 category B stations show clear Ps but only one of the multiples PpPs or PpSs + PsPs, so an optimal pair of (H, k) is less well determined. Even though we don't see the multiples as clearly as in category A stations, the results of nine of our category B stations agree well with the neighboring category A stations. For two stations in category B (EQ20 and EQ18) (Table 1) we had difficulty in finding optimum stacking parameters so we fixed the V_p/V_s at the value found for the intervening station (EQ19) for our estimation of Moho depth. For the 12 stations in category C, only the Ps but none of the multiples can be clearly observed, therefore H and k cannot be independently determined and are not shown in Table 1.

3.2. Velocity Depth Modeling via Neighborhood Algorithm

[19] The method applied here is a nonlinear inversion scheme, which requires a starting model that is iteratively improved using a sequence of relatively thin layers with a gradual increase or decrease of the velocity. For our initial V_s model, we used the average P wave velocity from the center of our refraction study [*Lerch et al.*, 2007] divided by 1.73 (assuming Poisson's ratio of 0.25) for all stations. Tests using different $V_s(z)$ starting models based on lateral variability of the refraction profile did not yield significant variations in the inversion.

[20] Before applying the inversion process, at each station the receiver functions were stacked for all available earthquakes to maximize the signal-to-noise ratio. We used receiver functions calculated from 5 s prior to the direct P wave arrival to 25 s after it. These time intervals include all crustal and lithospheric conversions as well as the strongest multiples. The observed receiver functions are inverted for the seismic velocity structure under each recording station using a neighborhood algorithm (NA) [*Sambridge*, 1999]. Each starting model is described by six layers with 24 parameters, the S velocity at the top and bottom of each layer, the thickness of the layer and the V_p/V_s ratio for the layer. Velocity gradients across each layer are represented by a "staircase" of uniform layers to aid the computation of the synthetic waveforms using a layer matrix method as in the work by *Shibutani et al.* [1996]. This neighborhood algorithm searches for the structure that produces a synthetic receiver function most closely fitting the observed waveform. It is an efficient method because the models tested are based on the results of previous models, so that more promising regions of the solution space are examined in more detail. In each iteration, 20 models are generated and synthetics are calculated for each. Then in the next iteration 20 new V(z) models are generated in the same way but now based on the best fitting model from the previous iteration.

[21] Progressive iterations of the neighborhood algorithm lead to a reduction of the misfit between the observed and synthetic waveforms, but overfitting the data leads to velocity depth functions that fluctuate wildly with depth. For our final models, we ran at least 500 iterations (10,000 V(z) models), then used visual inspection of additional iterations to stop the fitting process before the higher degree of fit led to seemingly implausible velocity depth functions. We modeled 1-D crustal structure below each station. Figure 6 shows the final velocity depth model obtained after 550 iterations of the receiver function inversion for our short-period station EQ3 (see Figure 1 for location).

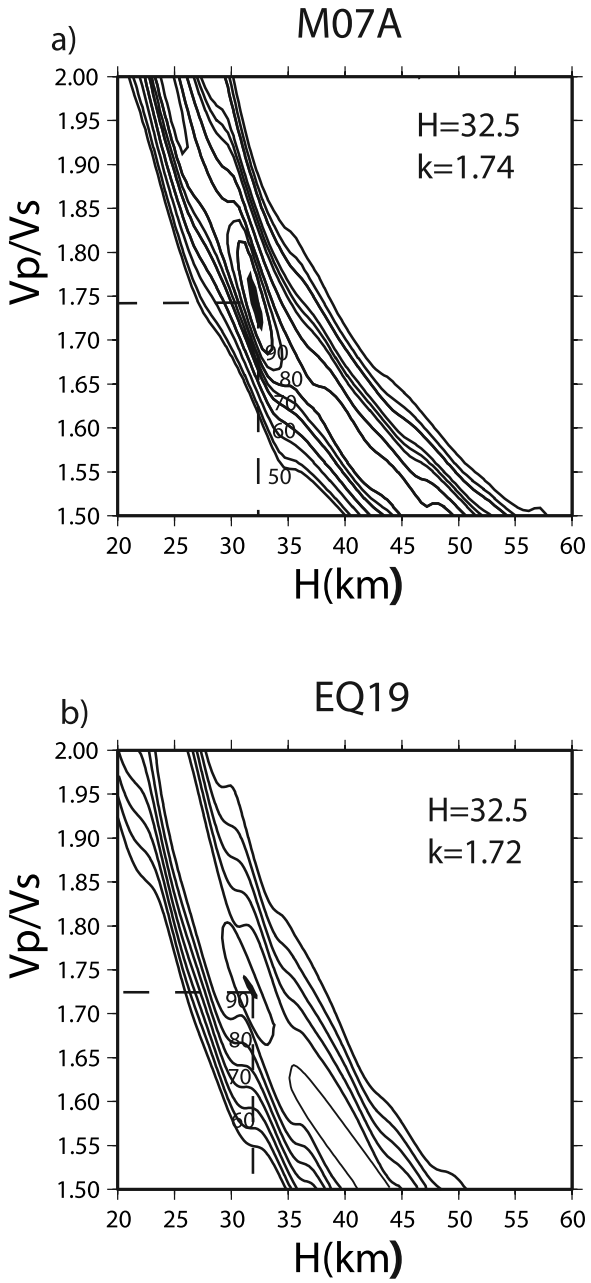

Figure 5. Example of the application of the *Zhu and Kanamori* [2000] H-k method at USArray broadband station M07A and short-period station EQ19. Contours are relative amplitudes normalized to the maximum stack value. The 95% contour is taken as our estimate of uncertainty in the picked value of H (mean crustal thickness) and k (mean crustal V_p/V_s).

[22] Receiver function inversions for shear wave velocity structure are nonunique as there is little absolute velocity information contained in the receiver functions, leading to a trade-off between velocity and depth. Inverse modeling is often affected by thin layers [*Xu et al.*, 2007] making it difficult to fit all the observed phases on the receiver function waveform. Although a combination of receiver function with surface wave phase velocity data [e.g., *Ozalaybey et al.*, 1997] should yield better absolute velocity information, for this study and for comparison with our wide-angle data we relied on the results of receiver functions alone.

3.3. Resolution and Uncertainty Estimates

[23] The horizontal resolution of receiver functions, that is, the area around the conversion point sampled by a receiver function, depends on the radius of the first Fresnel zone of the incident P wave [*Sheriff and Geldart*, 1995]. For a crust-mantle boundary at 32 km depth and average crustal velocity of $V_s \sim 3.7$ km s^{-1}, the radius of the corresponding Fresnel zone (assuming an incident P wave with a frequency of 0.3 Hz) is ~20 km. Our vertical resolution based on the quarter-wavelength criterion [*Sheriff and Geldart*, 1995] is ~3 km.

[24] Uncertainty in crustal thickness and V_p/V_s ratio from the *Zhu and Kanamori* [2000] grid search algorithm is on average $< \pm 1$ km and $< \pm 0.025$, respectively (Table 1), when defined as the region of H-k space in which stacked amplitude is >95% of the maximum. An additional source of uncertainty could come from uncertainty in the average crustal P velocity that is required as an input for the algorithm. For consistency, we assumed $V_p = 6.3$ km s^{-1} for all stations on the basis of refraction data [*Lerch et al.*, 2007]. The true average crustal P velocity for different stations may vary by ±0.2 km s^{-1}, corresponding to a change of crustal thickness of ±0.5 km.

4. Data and Results

[25] We processed data from 29 short-period stations and 5 broadband stations in our study area. Results of H-k stacking and velocity depth modeling of data are presented below.

4.1. Crustal Thickness and V_p/V_s Ratio

[26] For our study area, the V_p/V_s values from H-k stacking range from 1.68 to 1.83, with a mean of 1.76, and the crustal thickness ranges from 29.5 to 36.5 km, with a mean value of 33.0 km. Even the central short-period array alone, just ~70 km array length, shows V_p/V_s ratio varying from 1.68 to 1.76 and crustal thickness that varies from 30.5 to 34.0 km. Table 1 lists individual results and shows that the magnitude of the spatial variations of the parameters is significantly larger than the estimated uncertainty of most of the individual measurements, suggesting that lateral variation in properties is well constrained. Adjacent short-period stations yield crustal thickness and V_p/V_s estimates that overlap almost ubiquitously within error as expected given their small lateral spacing comparable to the seismic wavelength.

[27] Using the neighborhood algorithm, crustal thickness beneath the western stations MO6C and MOD is 34.5 and 36.5 km with V_p/V_s ratios of 1.78 and 1.72 for the upper crust and 1.78 and 1.78 for the lower crust, respectively. At the eastern two USArray stations, we derive crustal thicknesses of 31 km and 30.5 km at M08A and M09A, respectively (Figure 7). Inverse modeling of the receiver function waveforms using the neighborhood algorithm and the Zhu and Kanamori method show comparable crustal thickness estimates for most of our stations (Figure 8). Applying the neighborhood algorithm is however advanta-

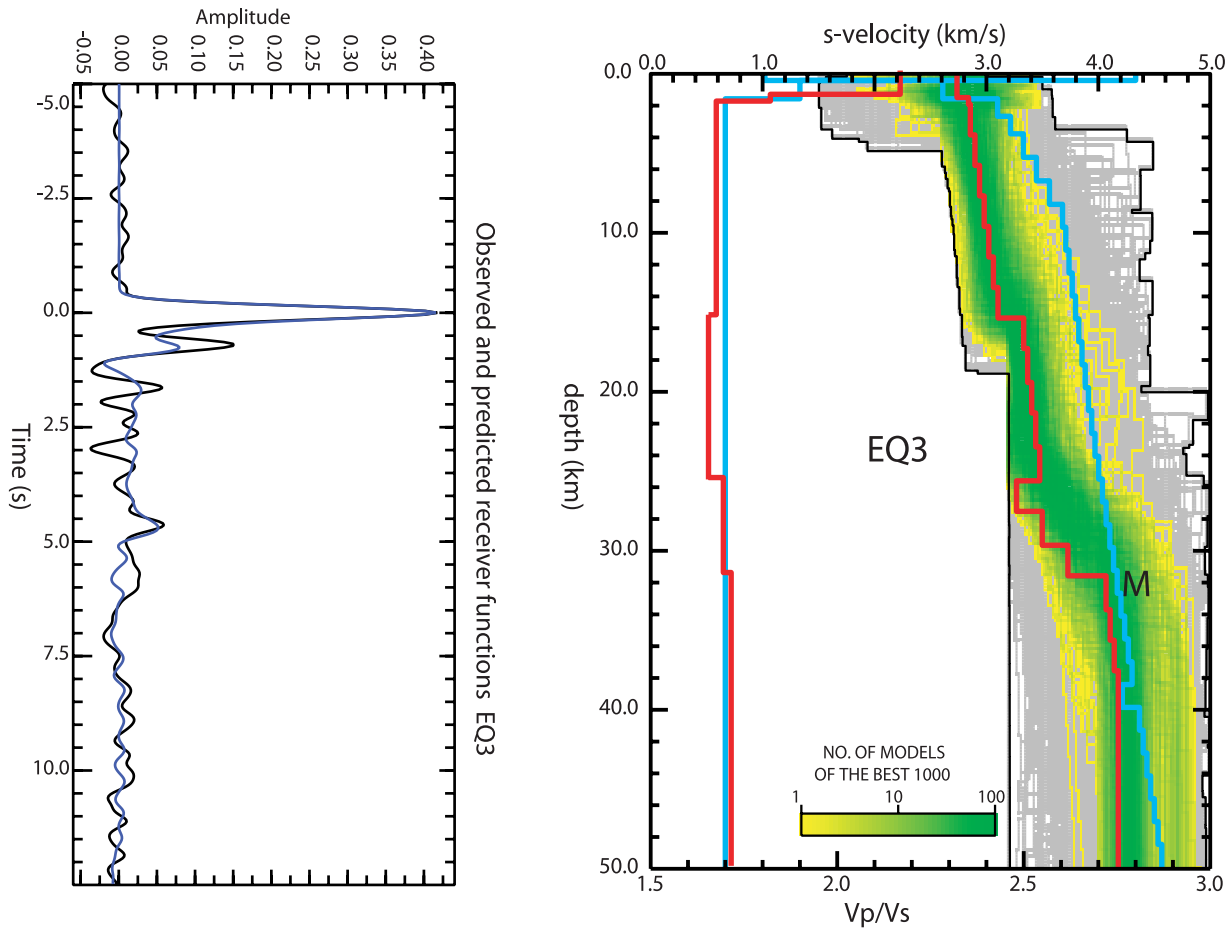

Figure 6. Neighborhood algorithm inversion at short-period station EQ3. (left) The observed (black line) and synthetic (blue line) receiver function waveforms. (right) The range of models searched in order to find the best fitting structure. The green regions indicate the models with better fit to the observations; the best fitting model is indicated by the red line that overlies the model density plot. The cyan lines superimposed on the model density plot are the starting V_s model and starting V_p/V_s ratio. The red lines are the best fitting V_s and V_p/V_s ratio model. Thin black lines bound the entire $V_s(z)$ space searched.

geous as it provides 1D variation of S velocity structure along with the variation of V_p/V_s with depth.

4.2. Regional Average and Spatial Trends in H and V_p/V_s

[28] The spatial variations in V_p/V_s are reasonably coherent across our study area, with eastern stations (on thinner crust) showing lower values than the western stations (Figure 8a and Table 1).

[29] We compared the bulk crustal properties determined from our H-k analysis with global compilations of V_p/V_s. *Christensen and Mooney* [1995] constructed a model of crustal petrology versus depth based on an extensive compilation of seismic profiling in conjunction with laboratory measurements of V_p. This model ranges from V_p/V_s of 1.74 in the upper crust to 1.81 in the lower crust, with an average value of 1.78. Our range of mean crustal values from 1.83 to 1.68 could be taken as showing a varying crustal composition from basaltic 50% SiO_2 to granitic 70% of SiO_2 [*Christensen*, 1996]. Although some studies of V_p/V_s [*Zandt and Ammon*, 1995], have suggested V_p/V_s increases with tectonothermal age, our highest V_p/V_s is observed in the youngest, westernmost crust (Figure 1), which must therefore be due to compositional effects (more mafic material) unrelated to age.

4.3. Comparison with Wide-Angle Refraction Data

[30] Passive array seismic data complement active source, wide-angle reflection/refraction profiling in several ways. Structures interpreted from teleseismic data are quite local to the array; refraction and wide-angle data entail potentially greater lateral ambiguity because of horizontal raypaths [*Jones and Phinney*, 1998]. Receiver functions yield information primarily about S wave velocity contrasts, thus leading to the possibility of inferring models of the crustal V_p/V_s ratio when combined with wide-angle reflection/refraction surveys that typically are dominated by P wave arrivals.

[31] In order to make comparisons of our receiver function crustal models with existing models from refraction profiles, we used our V_p/V_s ratio and our 1-D V_s velocity structure to calculate the P wave velocity beneath our 10 quality A stations. Figure 8c shows our resulting 1-D P wave velocity structure beneath these stations, which is

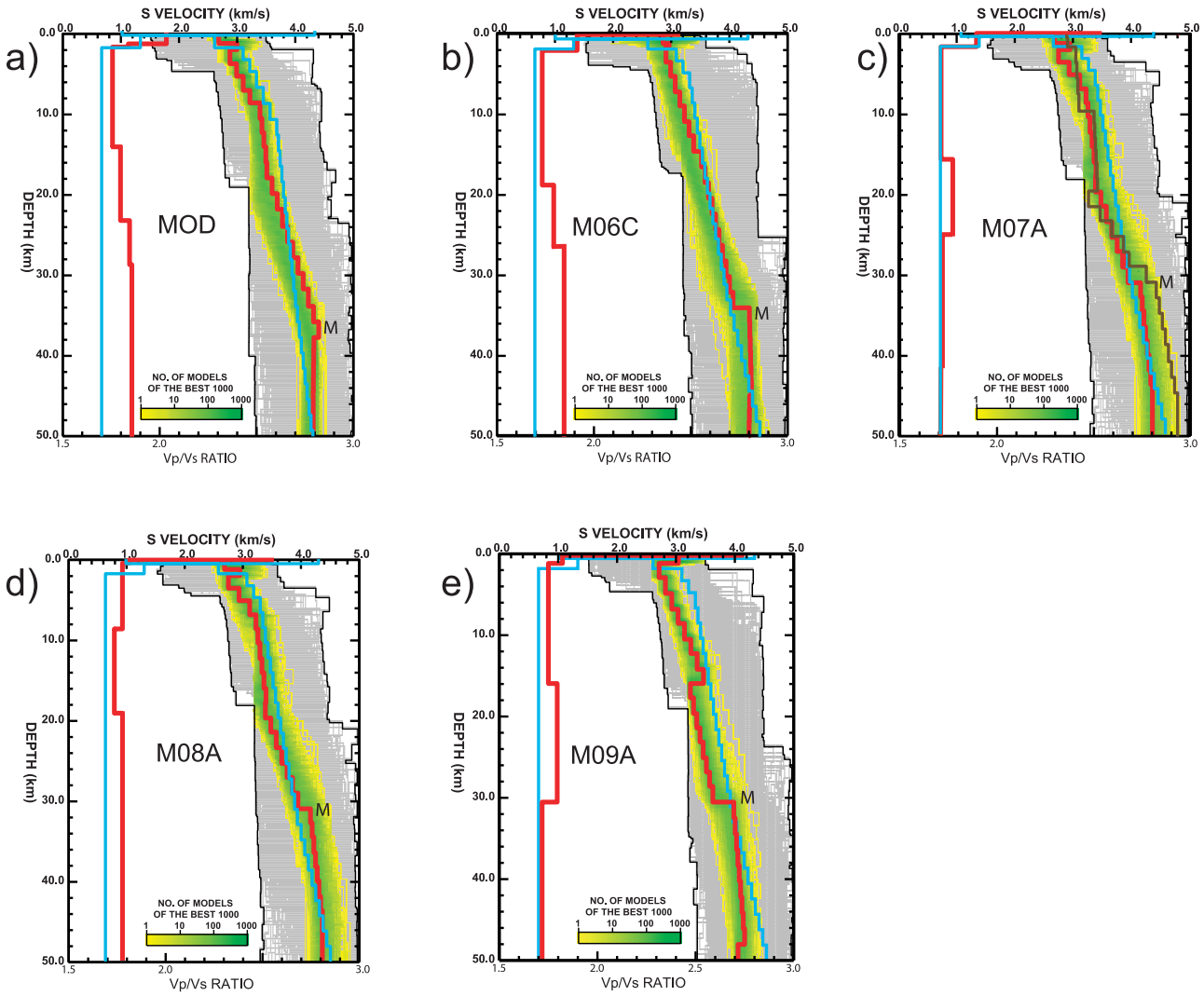

Figure 7. One-dimensional receiver function inversion results at five broadband stations west of ((a) MOD and (b) M06C), within ((c) M07A), and east of ((d) M08A and (e) M09A) the short-period array. For station M07A the brown line is the 1-D inversion using only the SE back azimuths where we observed a Moho doublet (Figure 3b). For additional explanation, see Figure 6.

broadly consistent with the refraction velocity [*Lerch et al.*, 2007] though our receiver function inversions tend to model higher velocities in the lower crust, vertically smearing out the crust-mantle velocity transition compared to the refraction model. Where the correlation between receiver function model and wide-angle models is poor, the mismatch could be due to differences in crustal structure between the location of the seismic stations and the projection point on the wide-angle model as our western stations are up to ~40 km north and south of the refraction line. More over, station spacing for the refraction survey is dense (100 m) whereas our short-period receiver function data was collected at ~2.5 km station interval hence wide-angle velocities are better resolved at the array center.

4.4. Composition of Crust Beneath Northwest Nevada

[32] We use our results described above to better constrain the composition and to discuss the evolution of the crust beneath the northwestern Basin and Range province. On the basis of the S velocity structure derived for our category A stations, we first divide the crust beneath this region into three layers (Figure 8b). Because there is no clear jump in velocities or change in gradient that is consistent between stations, we chose lines of equal velocity to divide the crust into layers. Our "upper crust" defined by a range in values of V_s of $2.8 \leq V_s \leq 3.2$ km s^{-1} extends from 2 km to ~10 km depth. We omitted the uppermost 2 km from our analysis to avoid or at least reduce the effect of sedimentary rocks. Our "middle crust", defined by $3.2 < V_s \leq 3.8$ km s^{-1}, extends from ~10 to ~23 km, and our deepest layer, the "lower crust", defined by $3.7 < V_s \leq 4.0$ km s^{-1}, lies roughly between 23 and 35 km.

[33] We compare our interpreted V_s and V_p/V_s ratio at each station with laboratory measurements of *Christensen* [1996]. When comparing laboratory data collected at room temperature with field-based measurements it is important to make pressure and temperature corrections. Changes in crustal seismic velocity as a function of temperature and pressure are generally assumed to be of the order of

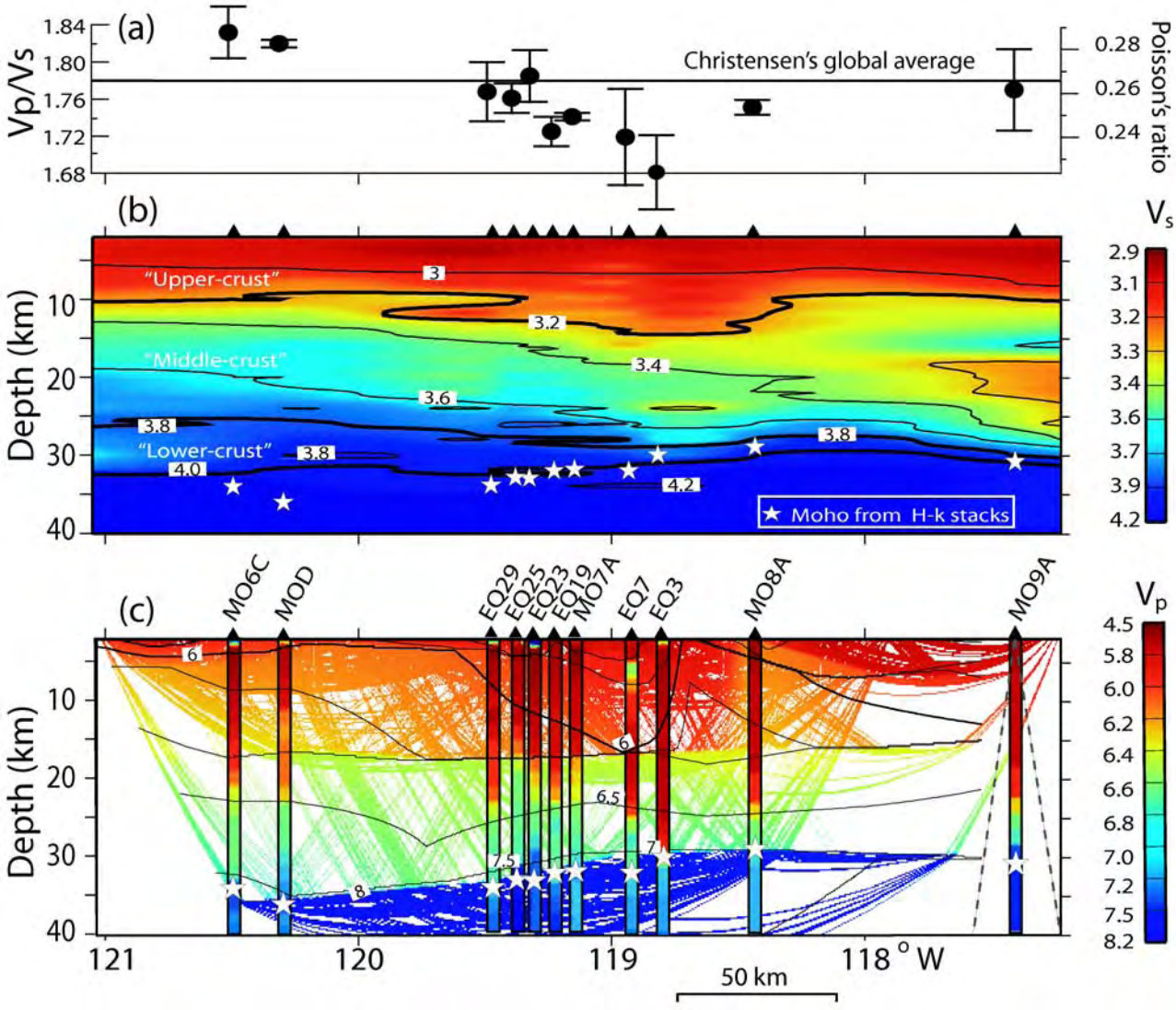

Figure 8. (a) V_p/V_s ratio for quality A stations from H-k analysis. (b) V_s structure below 2 km from the surface derived from category A stations by neighborhood inversion, overlain by Moho depth (stars) for these stations from H-k analysis. Velocity model is generalized into upper, middle, and lower crust and upper mantle separated by isovelocity contours at 3.2, 3.8 and 4.0 km s^{-1}. Vertical exaggeration is 3:1. (c) Comparison of velocity structure from 1-D receiver function inversion at quality A stations with wide-angle refraction results [*Lerch et al.*, 2007]. Receiver function velocities are $V_s(z)$ multiplied by $V_p/V_s(z)$, both taken from the neighborhood inversion (e.g., Figure 7). Dashed line (cone) beneath station M09A represents the actual sampled region for the receiver function results.

$\sim 4.10^{-4}$ km s^{-1} $^0C^{-1}$ and 2.10^{-4} km $s^{-1}MPa^{-1}$ for crustal rocks [*Rudnick and Fountain*, 1995]. No pressure correction was necessary because the laboratory measurements of *Christensen* [1996] are reported for appropriate confining pressures. Figures 9a, 9b and 9c show plots of V_p/V_s versus V_s for a wide variety of crustal and mantle rocks [*Christensen*, 1996] that might exist within our defined upper, middle and lower parts of crust, respectively, measured at 200, 600 and 800 MPa and corrected to temperatures of 300, 600 and 900°C.

[34] V_p/V_s and V_s for our quality A stations for the upper crust (Figure 9a) are grouped fairly tightly. There is a tendency toward higher values of V_p/V_s for the westernmost stations and eastern most stations, and the lowest V_p/V_s value is observed at station EQ3. Our data for the upper crust show velocities and V_p/V_s ratios lower than expected even for granites and metasedimentary rocks and may suggest the presence of sedimentary rocks [*Brocher*, 2005] below 2 km depth, or unusually quartz-rich basement lithologies. It is possible, but less likely, that the low observed V_s is caused by temperatures significantly above the 300°C that we used for the correction of seismic velocities.

[35] Our data show that both V_p/V_s and V_s tend to increase with depth, characteristic of more mafic lithologies, and also show a consistent variation from west to east (Figures 8a, 9b and 9c). For our western stations (MO6C, MOD and EQ29) we interpret an intermediate to mafic

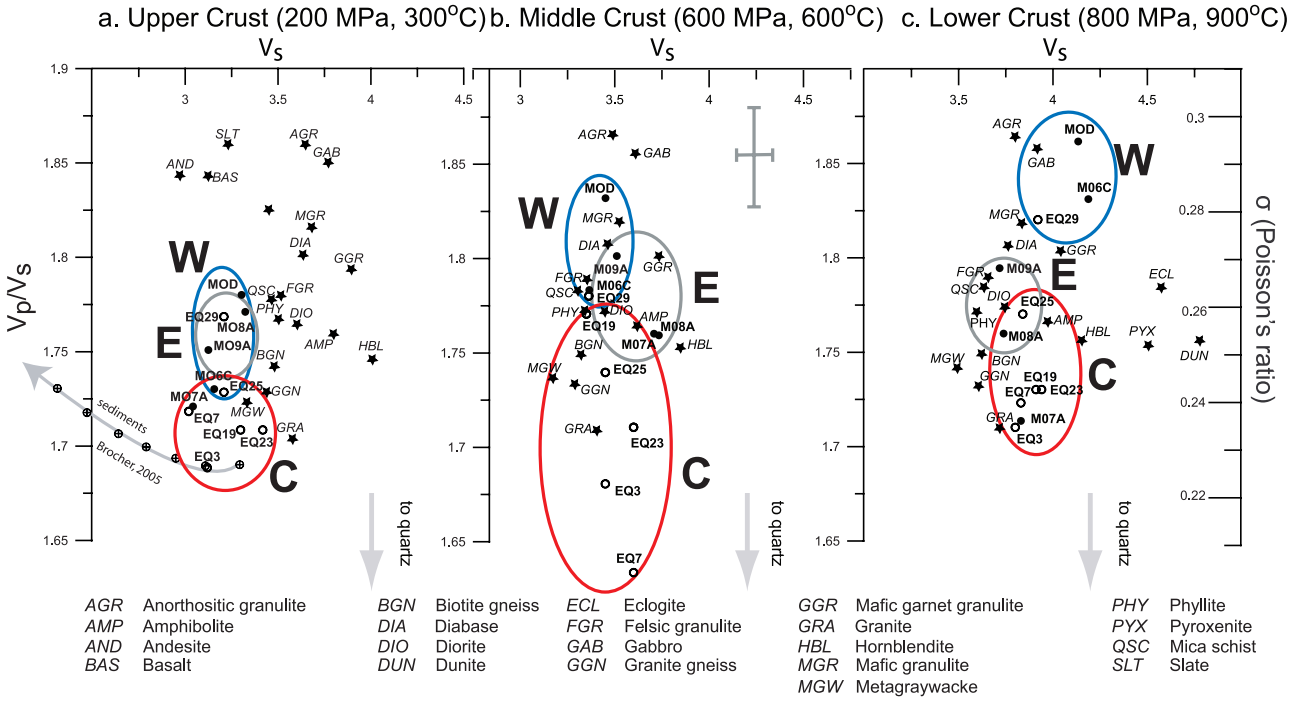

Figure 9. Plots of V_p/V_s versus V_s for laboratory measurements and our data. Black stars are data from *Christensen* [1996]. Open and filled circles are our inversion results for short-period and broadband stations, respectively, for (a) the upper crust, (b) the middle crust and (c) the lower crust. Three ellipses show the range of properties in western (W, blue line), central (C, gray line) and eastern (E, red line) stations, respectively. Gray arrows on the plot show trends due to sedimentary and quartz-rich lithologies. Three-letter abbreviations are rock names used by *Christensen* [1996]. Cross in Figure 9b shows typical range of values of V_s and V_p/V_s for rock samples grouped into a particular named category by *Christensen* [1996] and also serves as an estimate of uncertainty for our individual measurements.

middle crust (diabase to mafic granulite) and a mafic lower crust (mafic granulite to gabbro). In contrast, the central stations show unusually low V_p/V_s throughout the crust, both from the H-k stacking and from the layered neighborhood inversion. In particular, stations EQ3 and EQ7 have V_p/V_s ratios that lie in the lowest decile of the global survey of data by *Zandt and Ammon* [1995]. These stations sample a region of thickened upper and middle crust (Figure 8b) that also has unusually low upper crustal V_p from our wide-angle data (Figure 8c). We follow *Lerch et al.* [2007] in suggesting that the low V_p, low V_s and low V_p/V_s in this region mark the location of the Cretaceous Sierra Nevada felsic batholith in the subsurface. Immediately west of the low-velocity region we see a change in Moho character between EQ10 and EQ12 (Figure 4). We speculate that the change in Moho character may be related to the Mojave-Snow-Nevada-Idaho (MSNI) shear zone that acted as a major strike-slip fault accommodating several hundred km of offset in early Cretaceous time [*Wyld and Wright*, 2007] that outcrops just 10 km east of EQ10 [*Wyld and Wright*, 2001] (Figure 1). We recognize that this interpretation is potentially at odds with nearby data thought to show widespread Cenozoic magmatic or structural overprints of older features [e.g., *Klemperer et al.*, 1986; *McKenzie et al.*, 2000]. Nonetheless, the MSNI may broadly be following the line of the Sierra Nevada-Idaho batholith system, that as an active arc would have been a relatively weak zone inboard of the continental edge in Cretaceous time.

[36] Just 40 km to the west there is a significant increase in V_p/V_s between EQ19 and EQ23 (Table 1). All our category A stations yet further west have V_p/V_s close to or in excess of the continental average ($V_p/V_s \sim 1.77$), with the two western stations (MOD and MO6C) showing the highest values. It is possible that the high V_p/V_s values represent mafic additions throughout the crust associated with the young basalts of the Modoc and Sheldon plateaus, though there is no evidence for such additions increasing to the west, and the Tertiary volcanic outcrop of the Sheldon Plateau also extends east across the area of low V_p/V_s seen on EQ7 and EQ3. A likely alternative explanation is that the mafic rocks represented by the high V_p/V_s ratios are part of accreted Paleozoic island arcs similar to those exposed in the eastern Klamath and northwestern Sierra Nevada. If so, mafic arc terranes may form the basement to a broad region of northeast California and northwest Nevada [*Dickinson*, 2000].

[37] Even though the orientation of our array was designed to assess variation of crustal properties from west to east, studying the back azimuthal variation of receiver functions allowed us to identify a Moho doublet from the SE back azimuth (e.g., Figure 3b). Neighborhood algorithm modeling of receiver functions from this azimuth suggests a 5–7 km thick lower crustal layer with V_s ~4.1 km s^{-1} (Figure 7c). This layer is perhaps related to the discrete lower crustal "7.*x*" km s^{-1} layer, commonly attributed to the presence of magmatic underplating [e.g., *Catchings*,

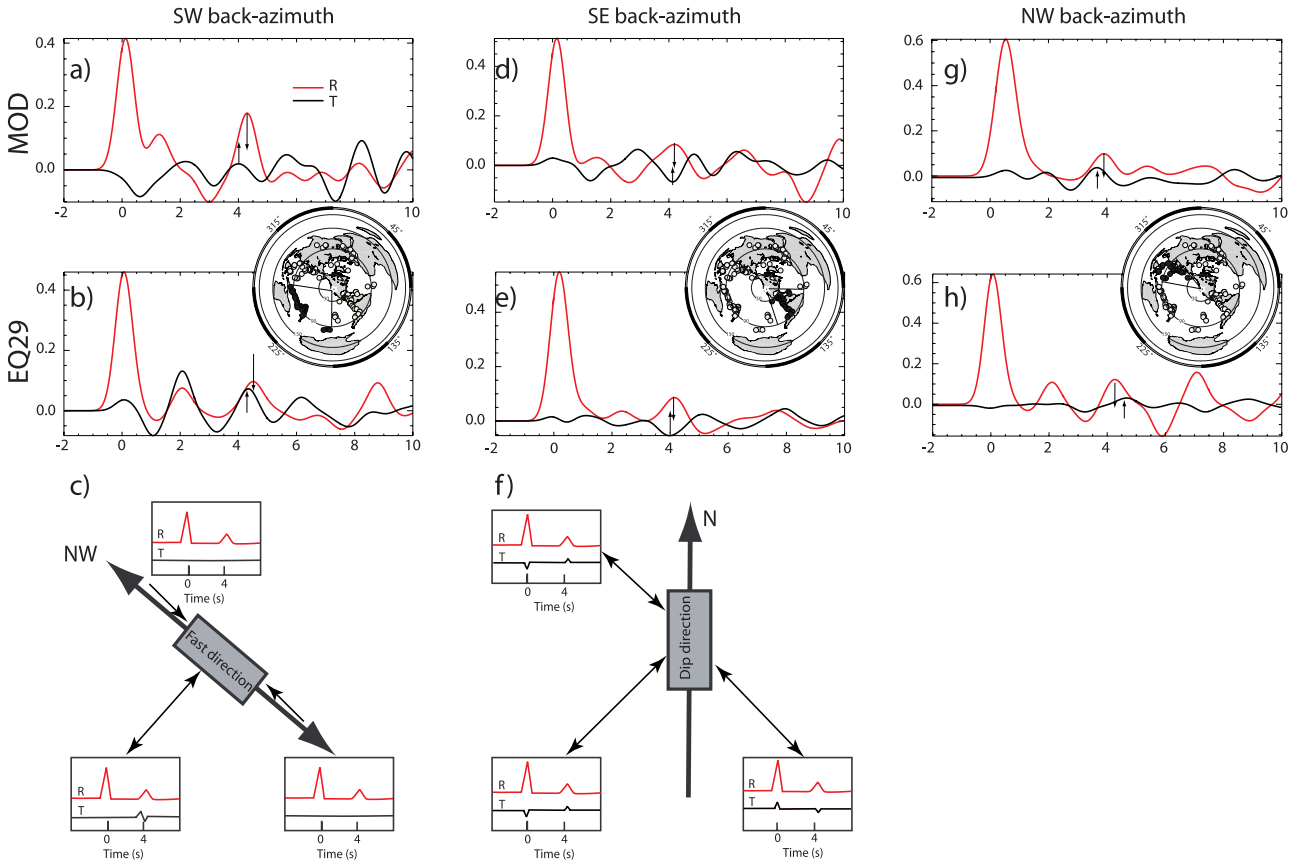

Figure 10. Receiver function stacks for the radial (red) and transverse (black) receiver functions at stations MOD and EQ29 plotted at the same scale. Back azimuthal stacks are for (a and b) southwest events, (d and e) southeast events and (g and h) northwest events. The inset maps indicate the earthquakes producing the receiver functions stacked to produce each pair of data plots (MOD and EQ29). In Figures 10a and 10b the radial Moho Ps conversion arrives slightly later than the tangential Moho Ps conversion, indicating influence due to anisotropy. (c) Schematic predictions for receiver functions as a function of back azimuth resulting from NW-SE fast anisotropy. In Figures 10d and 10e the radial and tangential Moho Ps phase arrives at the same time but with opposite polarity indicative of dipping Moho. (f) Schematic predictions of receiver functions resulting from a north dipping Moho. Observed tangential energy in Figures 10g and 10h is minimum for northwest back azimuths. Figures 10c and 10f are redrawn after *Peng and Humphreys* [1997].

1992] and to a zone of enhanced near-vertical reflectivity at the base of the crust [*Klemperer et al.*, 1986]. Although *Lerch et al.* [2007] limited the thickness of this lower crustal layer to <3 km from amplitude modeling of our wide-angle refraction data, our broadband stations recorded Moho conversions up to ~30 km offline, thus sampling the lower crust significantly away from the refraction line.

4.5. Moho Dip and Crustal Anisotropy

[38] Thus far we have implicitly assumed an isotropic seismic structure of the crust and upper mantle composed of flat-lying planar interfaces. Clearly these assumptions are imperfect [*Ammon*, 1992; *Bank and Bostock*, 2003; *Savage*, 1998; *Vinnik and Montagner*, 1996]. Predictable back azimuthal variations in timing and amplitude of teleseismic-converted phases allow recognition of more complicated features such as dipping interfaces or anisotropic fabrics. In particular, any departure from an Earth consisting of flat homogenous isotropic layers should produce significant tangential energy that can be explained by planar dipping interfaces or anisotropy [*Langston*, 1977].

[39] We calculated the transverse receiver function in the same manner described previously for the radial receiver functions, but this time we deconvolved the transverse component from the vertical. Our data has observable tangential energy, albeit significantly lower amplitude than the radial component (Figure 10). To understand the effect of dip and anisotropy on our receiver functions, we compared radial and tangential receiver functions at different back azimuths (Figure 10).

[40] In our data, modest amplitude tangential energy slightly advanced in time from the radial energy is typically observed for events arriving from southwestern back azimuths (Figures 10a and 10b) whereas minimal tangential energy is observed for events coming from northwest azimuths (Figures 10g and 10h). This would suggest that the axis of anisotropy is oriented roughly NW-SE (Figure 10c). Although the magnitude of extension in our

region is small at the surface [*Colgan et al.*, 2006], it has a similar fast direction to that recognized ~100 km south of our array [*McNamara and Owens*, 1993]. This fast direction is likely due to an anisotropic crustal fabric caused by lower crustal flow driven by NW-SE oriented Cenozoic extension [e.g., *Parsons*, 1995].

[41] We clearly observe increased Moho depth toward our western stations from the 1D inversion (Figures 7 and 8). Close analysis of our tangential receiver function stacks from southeastern azimuths shows tangential Ps energy arriving at the same time as the radial energy with opposite polarity (Figures 10d and 10e). This pattern is suggestive of a north dipping Moho (Figure 10f) as might be expected from our experiment location on the northern margin of the extended Basin and Range province.

5. Conclusions

[42] We combined teleseismic waveform data from a PASSCAL short-period seismic network and broadband stations of the USArray transportable array to determine crustal thickness variations and rock properties beneath the northwest Basin and Range region. Our results show a general trend of westward crustal thickening from 29.5 km in the east to 36.5 km in the west across the western boundary of the Basin and Range province. Although the USArray data are better than the short-period data both because of higher signal-to-noise and generally longer recording times, the short-period sensors also produced receiver functions that show the same crustal thickening. With 8 months data, 20% of our short-period stations gave good H-k results (category A stations) and 30% gave adequate results (category B). Thus these short-period sensors may supplement and densify broadband arrays, but cannot easily replace them.

[43] The two inversion techniques we employed, the H-k [*Zhu and Kanamori*, 2000] and neighborhood algorithm [*Sambridge*, 1999] methods, demonstrate regional trends of bulk crustal properties and of the vertical variation of these properties with depth as we go from the more extended parts of the Nevada Basin and Range province to the less extended volcanic plateau further west.

[44] In summary we find (1) lower V_p/V_s in the upper crust than in the lower crust as is commonly observed worldwide; (2) mean crustal V_p/V_s of the Modoc plateau (MOD and MO6C) of ~1.82 that is clearly above the global continental average presumably documenting crust that is more mafic than average; and (3) mean crustal V_p/V_s of a narrow zone in northwestern Nevada of ~1.72, clearly below the global mean, which we believe marks the location of the Cretaceous Sierra Nevada batholith. We also found a northward Moho dip (Figure 10d) from our receiver function data and a NW-SE oriented crustal anisotropy (Figure 10c) consistent with the dominant NW-SE oriented Cenozoic extension direction

[45] The receiver function technique, even with short-period stations, is an effective tool to constrain Moho depth, and the variation of V_p/V_s with depth. Comparisons of our receiver function crustal models with existing models from our wide-angle refraction profile show a reasonable correlation in terms of crustal thickness. Although the absolute crustal velocities from the receiver function technique are not so well resolved as from the wide-angle profile, the receiver function technique provides V_s data, which in combination with the wide-angle V_p, allow better interpretation of crustal lithology.

[46] **Acknowledgments.** We thank Derek Lerch and Joe Colgan for assisting with the field deployment. Field support and instruments for the experiment were provided by the PASSCAL Instrument Center. Funding for passive-source deployments came from Stanford University and for the wide-angle profiling from NSF-Earthscope grant 0346245 and by the Petroleum Research Fund of The American Chemical Society grant 39063-AC8. We thank Malcolm Sambridge for making the neighborhood algorithm code available for public use. Detailed review by Matthew Fouch and anonymous reviewer has greatly improved the manuscript. All seismic data are available through the IRIS DMC.

References

Allmendinger, R. W., T. A. Hauge, E. C. Hauser, C. J. Potter, S. L. Klemperer, K. D. Nelson, P. L. K. Knuepfer, and J. Oliver (1987), Overview of the COCORP 40°N transect, western United States: The fabric of an orogenic belt, *Geol. Soc. Am. Bull.*, *98*, 308–319, doi:10.1130/0016-7606(1987)98<308:OOTCNT>2.0.CO;2.

Ammon, C. J. (1992), A comparison of deconvolution techniques, *Tech. Rep. UCID-ID-111667*, Lawrence Livermore Natl. Lab., Livermore, Calif.

Bank, C. G., and M. G. Bostock (2003), Linearized inverse scattering of teleseismic waves for anisotropic crust and mantle structure: 2. Numerical examples and application to data from Canadian National Network stations, *J. Geophys. Res.*, *108*(B5), 2259, doi:10.1029/2002JB001951.

Barton, M. D., and R. B. Hanson (1989), Magmatism and the development of low-pressure metamorphic belts: Implications from the western United States and thermal modeling, *Geol. Soc. Am. Bull.*, *101*, 1051–1065, doi:10.1130/0016-7606(1989)101<1051:MATDOL>2.3.CO;2.

Blackwell, D. D., J. L. Steele, and L. S. Carter (1991), Heat flow patterns of the North American continent: A discussion of the Decade of North American Geology geothermal map of North America, in *Neotectonics of North America*, edited by D. B. Slemmons et al., pp. 423–436, Geol. Soc. of Am., Boulder, Colo.

Brocher, T. (2005), Empirical relations between elastic wave-speeds and density in the Earth's crust, *Bull. Seismol. Soc. Am.*, *95*, 2081–2092, doi:10.1785/0120050077.

Buck, W. R. (1991), Modes of continental extension, *J. Geophys. Res.*, *96*, 20,161–20,178, doi:10.1029/91JB01485.

Burchfiel, B. C., and G. A. Davis (1975), Nature and controls of Cordilleran orogenesis in the western United States: Extensions of an earlier synthesis, *Am. J. Sci.*, *275A*, 363–396.

Burchfiel, B. C., D. S. Cowan, and G. A. Davis (1992), Tectonic overview of the Cordilleran orogen in the western U. S., in *The Geology of North America, The Cordilleran Orogen: Conterminous U. S.*, vol. G3, edited by Burchfiel et al., pp. 407–480, Geol. Soc. Of Am., Boulder, Colo.

Catchings, R. D. (1992), A relation among geology, tectonics, and velocity structure, western to central Nevada Basin and Range, *Geol. Soc. Am. Bull.*, *104*, 1178–1192, doi:10.1130/0016-7606(1992)104<1178:ARAGTA>2.3.CO;2.

Catchings, R. D., and W. D. Mooney (1991), Basin and Range crustal and upper mantle structure of northwest to central Nevada, *J. Geophys. Res.*, *96*, 6247–6267, doi:10.1029/91JB00194.

Christensen, N. I. (1996), Poisson's ratio and crustal seismology, *J. Geophys. Res.*, *101*, 3139–3156, doi:10.1029/95JB03446.

Christensen, N. I., and W. D. Mooney (1995), Seismic velocity structure and composition of the continental crust: A global view, *J. Geophys. Res.*, *100*, 9761–9788, doi:10.1029/95JB00259.

Christiansen, R. L., and R. S. Yeats (1992), Post-Laramide geology of the U. S. Cordilleran region, in *The Geology of North America, The Cordilleran Orogen: Conterminous U. S.*, vol. G3, edited by B. C. Burchfiel et al., pp. 407–480, Geol. Soc. of Am., Boulder, Colo.

Colgan, J. P., T. A. Dumitru, E. L. Miller, and P. R. Reiners (2006), Cenozoic tectonic evolution of the Basin and Range province in northwestern Nevada, *Am. J. Sci.*, *306*, 616–654, doi:10.2475/08.2006.02.

Dalziel, I. W. D. (1997), Neoproterozoic-Paleozoic geography and tectonics: Review, hypothesis, environmental speculations, *Geol. Soc. Am. Bull.*, *109*, 16–42, doi:10.1130/0016-7606(1997)109<0016:ONPGAT>2.3.CO;2.

Dickinson, W. R. (2000), Geodynamic interpretation of Paleozoic tectonic trends oriented oblique to the Mesozoic Klamath-Sierran continental margin in California, in *Paleozoic and Triassic Paleogeography and Tectonics of Western Nevada and Northern California*, edited by M. J. Soreghan and G. Gehrels, Spec. Pap. Geol. Soc. Am., *347*, 209–246.

Holbrook, W. S. (1990), The crustal structure of the northwestern Basin and Range province, Nevada, from wide-angle seismic data, *J. Geophys. Res.*, *95*, 21,843–21,869, doi:10.1029/JB095iB13p21843.

Jones, C. H., and R. A. Phinney (1998), Seismic structure of the lithosphere from teleseismic converted arrivals observed at small arrays in the southern Sierra Nevada and vicinity, California, *J. Geophys. Res.*, *103*, 10,065–10,090, doi:10.1029/97JB03540.

Kern, H. (1982), Elastic-wave velocity in crustal and mantle rocks at high pressure and temperature: The role of the high-low quartz transition and of dehydration reactions, *Phys. Earth Planet. Inter.*, *29*, 12–23, doi:10.1016/0031-9201(82)90133-9.

Kistler, R. W. (1990), Two different lithosphere types in the Sierra Nevada, California, in *The Nature and Origin of Cordilleran Magmatism*, edited by J. L. Anderson, *Mem. Geol. Soc. Am.*, *174*, 271–281.

Kistler, R. W., and Z. E. Peterman (1978), Reconstruction of crustal blocks of California on the basis of initial strontium isotopic compositions of Mesozoic granitic rocks, *U. S. Geol. Surv. Prof. Pap.*, *1071*, 17.

Klemperer, S. L., T. A. Hauge, E. C. Hauser, J. E. Oliver, and C. J. Potter (1986), The Moho in the northern Basin and Range province, Nevada, along the COCORP 40°N seismic-reflection transect, *Geol. Soc. Am. Bull.*, *97*, 603–618, doi:10.1130/0016-7606(1986)97<603:TMITNB>2.0.CO;2.

Langston, C. A. (1977), Effect of planar dipping structure on source and receiver responses for constant ray parameter, *Bull. Seismol. Soc. Am.*, *67*, 1029–1050.

Langston, C. A. (1979), Structure under Mount Rainier,Washington, inferred from teleseismic body waves, *J. Geophys. Res.*, *84*, 4749–4762, doi:10.1029/JB084iB09p04749.

Lerch, D. W., S. L. Klemperer, J. M. G. Glen, D. A. Ponce, E. L. Miller, and J. P. Colgan (2007), Crustal structure of the northwestern Basin and Range Province and its transition to unextended volcanic plateaus, *Geochem. Geophys. Geosyst.*, *8*, Q02011, doi:10.1029/2006GC001429.

Ligorria, J. P., and C. J. Ammon (1999), Iterative deconvolution and receiver-function estimation, *Bull. Seismol. Soc. Am.*, *89*, 1395–1400.

Miller, E., J. Wright, and R. Madrid (1992), Late Paleozoic paleogeographic and tectonic evolution of the western U. S. Cordillera, in *The Geology of North America, The Cordilleran Orogen: Conterminous U. S.*, vol. G3, edited by B. Burchfiel et al., pp. 57–106, Geol. Soc. of Am., Boulder, Colo.

McKenzie, D., F. Nimmo, J. A. Jackson, P. B. Gans, and E. L. Miller (2000), Characteristics and consequences of flow in the lower crust, *J. Geophys. Res.*, *105*, 11,029–11,046, doi:10.1029/1999JB900446.

McNamara, D. E., and T. J. Owens (1993), Azimuthal shear-wave velocity anisotropy in the Basin and Range Province using Moho Ps converted phases, *J. Geophys. Res.*, *98*, 12,003–12,017, doi:10.1029/93JB00711.

Owens, T. J. (1987), Crustal structure of the Adirondacks determined from broadband teleseismic waveform modeling, *J. Geophys. Res.*, *92*, 6391–6401, doi:10.1029/JB092iB07p06391.

Ozalaybey, S., M. K. Savage, A. F. Sheehan, J. N. Louie, and J. N. Brune (1997), Shear wave velocity structure in the northern Basin and Range province from the combined analysis of receiver functions and surface waves, *Bull. Seismol. Soc. Am.*, *87*, 183–199.

Parsons, T. (1995), The Basin and Range Province, in *Continental Rifts: Evolution, Structure and Tectonics*, edited by K. Olsen, pp. 277–324, Elsevier, Amsterdam.

Peng, X. H., and E. D. Humphreys (1997), Moho dip and crustal anisotropy in northwestern Nevada from teleseismic receiver functions, *Bull. Seismol. Soc. Am.*, *87*, 745–754.

Phinney, R. A. (1964), Structure of the Earth's crust from spectral behavior of long-period body waves, *J. Geophys. Res.*, *69*, 2997–3017, doi:10.1029/JZ069i014p02997.

Pierce, K. L., L. A. Morgan, and R. W. Saltus (2002), Yellowstone plume head: Postulated tectonic relations to the Vancouver slab, continental boundaries, and climate, in *Tectonic and Magmatic Evolution of the Snake River Plain Volcanic Province: Idaho*, edited by B. Bonnichsen et al., U. S. Geol. Surv. Bull., *30*, 5–33.

Potter, C. J., C. S. Liu, J. Huang, L. Zheng, T. A. Hauge, E. C. Hauser, R. W. Allmendinger, J. E. Oliver, S. Kaufman, and L. Brown (1987), Crustal structure of north-central Nevada from COCORP deep seismic reflection profiling, *Geol. Soc. Am. Bull.*, *98*, 330–337, doi:10.1130/0016-7606(1987)98<330:CSONNR>2.0.CO;2.

Priestley, K. F., and J. N. Brune (1978), Surface waves and the structure of the Great Basin of Nevada and western Utah, *J. Geophys. Res.*, *83*, 2265–2272, doi:10.1029/JB083iB05p02265.

Priestley, K. F., and J. N. Brune (1982), Shear wave structure of the southern volcanic plateau of Oregon and Idaho and the northern Great Basin of Nevada from surface wave dispersion, *J. Geophys. Res.*, *87*, 2671–2675, doi:10.1029/JB087iB04p02671.

Priestley, K. F., J. A. Orcutt, and J. N. Brune (1980), Higher mode surface waves and the structure of the Great Basin of Nevada and western Utah, *J. Geophys. Res.*, *85*, 7166–7174, doi:10.1029/JB085iB12p07166.

Ramesh, D. S., R. Kind, and X. Yuan (2002), Receiver function analysis of the North American crust and upper mantle, *Geophys. J. Int.*, *150*, 91–108, doi:10.1046/j.1365-246X.2002.01697.x.

Rudnick, R. L., and D. M. Fountain (1995), Nature and composition of the continental crust: A lower crustal perspective, *Rev. Geophys.*, *33*, 267–310, doi:10.1029/95RG01302.

Salisbury, M. H., and D. M. Fountain (1993), The seismic velocity and Poisson's ratio structure of the Kapuskasing Uplift from laboratory measurements, *Can. J. Earth Sci.*, *31*, 1052–1063.

Sambridge, M. S. (1999), Geophysical inversion with a neighbourhood algorithm: I. Searching a parameter space, *Geophys. J. Int.*, *138*, 479–494, doi:10.1046/j.1365-246X.1999.00876.x.

Savage, M. K. (1998), Lower crustal anisotropy or dipping boundaries? Effects on receiver functions and a case study in New Zealand, *J. Geophys. Res.*, *103*, 15069–15,087, doi:10.1029/98JB00795.

Sheriff, R., and L. Geldart (1995), *Exploration Seismology*, 2nd ed., 592 pp., Cambridge Univ. Press, Cambridge, U. K.

Shibutani, T., M. Sambridge, and B. Kennett (1996), Genetic algorithm inversion for receiver functions with application to crust and upper mantle structure beneath eastern Australia, *Geophys. Res. Lett.*, *23*, 1829–1832, doi:10.1029/96GL01671.

Tarkov, A. P., and V. V. Vavakin (1982), Poisson's ratio behaviour in crystalline rocks: Application to the study of the Earth's interior, Phys, *Earth Planet. Inter.*, *29*, 24–29, doi:10.1016/0031-9201(82)90134-0.

Taylor, S. R., and H. J. Patton (1986), Shear-velocity structure from regionalized surface-wave dispersion in the Basin and Range, *Geophys. Res. Lett.*, *13*, 30–33, doi:10.1029/GL013i001p00030.

Thatcher, W., G. R. Foulger, B. R. Julian, J. Svarc, E. Quilty, and G. W. Bawden (1999), Present-day deformation across the Basin and Range Province, western United States, *Science*, *283*, 1714–1718, doi:10.1126/science.283.5408.1714.

Vinnik, L. P. (1977), Detection of waves converted from P to SV in the mantle, *Phys. Earth Planet. Inter.*, *15*, 39–45, doi:10.1016/0031-9201(77)90008-5.

Vinnik, L., and J. P. Montagner (1996), Shear wave splitting in the mantle *Ps* phases, *Geophys. Res. Lett.*, *23*, 2449–2452, doi:10.1029/96GL02263.

Watanabe, T. (1993), Effects of water and melt on seismic velocities and their application to characterization of seismic reflectors, *Geophys. Res. Lett.*, *20*, 2933–2936, doi:10.1029/93GL03170.

Wyld, S. J., and J. E. Wright (2001), New evidence for Cretaceous strike-slip faulting in the U. S. Cordillera and implications for terrane displacement, deformation patterns and plutonism, *Am. J. Sci.*, *301*, 150–181.

Wyld, S. J., and J. E. Wright (2007), Alternative tectonic model for Late Jurassic through Early Cretaceous evolution of the Great Valley Group, California, in *Convergent Margin Terranes and Associated Regions: A Tribute to W. G. Ernst,* edited by M. Cloos et al., *Spec. Pap. Geol. Soc. Am.*, *419*, 1–15.

Xu, L., S. Rondenay, and R. D. van der Hilst (2007), Structure of the crust beneath the southeastern Tibetan Plateau from teleseismic receiver functions, *Phys. Earth Planet. Inter.*, *165*, 176–193.

Zandt, G., and C. J. Ammon (1995), Continental crust composition constrained by measurements of crustal Poisson's ratio, *Nature*, *374*, 152–154, doi:10.1038/374152a0.

Zandt, G., and T. J. Owens (1986), Comparison of crustal velocity profiles determined by seismic refraction and teleseismic methods, *Tectonophysics*, *128*, 155–161, doi:10.1016/0040-1951(86)90317-3.

Zhu, L., and H. Kanamori (2000), Moho depth variation in southern California from teleseismic receiver functions, *J. Geophys. Res.*, *105*, 2969–2980, doi:10.1029/1999JB900322.

E. M. Gashawbeza and S. L. Klemperer, Department of Geophysics, Stanford University, 397 Panama Mall, Mitchell Building, Stanford, CA 94305, USA.

E. L. Miller, Department of Geological and Environmental Sciences, Stanford University, 450 Serra Mall, Braun Hall, Building 320, Stanford, CA 94305, USA.

C. K. Wilson, Marsico Capital Management, 1200 17th Street, Suite 1600, Denver, CO 80202, USA.